Pathway and mechanism of drug binding to G-protein-coupled receptors

Ron O. Dror[a,1,2], Albert C. Pan[a,1], Daniel H. Arlow[a,1], David W. Borhani[a], Paul Maragakis[a], Yibing Shan[a], Huafeng Xu[a], and David E. Shaw[a,b,2]

[a]D. E. Shaw Research, New York, NY 10036; and [b]Center for Computational Biology and Bioinformatics, Columbia University, New York, NY 10032

Edited by Robert J. Lefkowitz, Duke University Medical Center/Howard Hughes Medical Institute, Durham, NC, and approved June 2, 2011 (received for review March 22, 2011)

How drugs bind to their receptors—from initial association, through drug entry into the binding pocket, to adoption of the final bound conformation, or "pose"—has remained unknown, even for G-protein-coupled receptor modulators, which constitute one-third of all marketed drugs. We captured this pharmaceutically critical process in atomic detail using the first unbiased molecular dynamics simulations in which drug molecules spontaneously associate with G-protein-coupled receptors to achieve final poses matching those determined crystallographically. We found that several beta blockers and a beta agonist all traverse the same well-defined, dominant pathway as they bind to the β_1- and β_2-adrenergic receptors, initially making contact with a vestibule on each receptor's extracellular surface. Surprisingly, association with this vestibule, at a distance of 15 Å from the binding pocket, often presents the largest energetic barrier to binding, despite the fact that subsequent entry into the binding pocket requires the receptor to deform and the drug to squeeze through a narrow passage. The early barrier appears to reflect the substantial dehydration that takes place as the drug associates with the vestibule. Our atomic-level description of the binding process suggests opportunities for allosteric modulation and provides a structural foundation for future optimization of drug–receptor binding and unbinding rates.

dewetting | kinetics | ligands | drug target | alprenolol

Systematic determination of drug efficacy dates to Ehrlich's experiments that culminated in the discovery of the first chemotherapeutic "magic bullet," Salvarsan. In the ensuing century, such measurements of drug efficacy and—once the molecular targets of drugs, or "receptors," were identified—of drug–receptor affinity have become de rigueur (1, 2). Affinity measurements are increasingly augmented by characterization of the kinetics of drug–receptor interaction, for several reasons: fast drug binding increases opportunities to capture transiently accessible receptor conformations; fast unbinding may confer safety advantages; and slow unbinding leads to long drug–receptor residence times that can dramatically enhance therapeutic efficacy at equivalent affinity (3, 4).

In stark contrast, essentially nothing is known about the process by which drugs bind to their receptors. By what pathway, or pathways, do drugs enter and exit the receptor binding pocket? Must drugs first associate with regions outside the binding pocket to bind? Might drugs sometimes bind (perhaps transiently) in more than one orientation or conformation within the binding pocket? Additionally, what factors determine binding and unbinding rates? Despite the innovative variety of experimental and computational techniques that have been applied to study binding mechanisms (5–16), these questions have proven extremely difficult to address, in part because they involve unstable structural states that are occupied only transiently.

G-protein-coupled receptors (GCPRs) represent the largest class of drug targets, and one-third of all drugs act by binding to GCPRs. Recent advances have yielded crystal structures that reveal the dominant GPCR-bound conformations, or "poses," of several drugs and related ligands (17). These ligands all lie buried within a deep binding pocket—the canonical "orthosteric" site that is cradled within a characteristic bundle of seven transmembrane helices—that is typically accessed from the extracellular side of the receptor. These advances have left unresolved, however, both the process by which drugs bind to GPCRs and the precise location and nature of alternative, allosteric binding sites (18).

Here, we used unbiased molecular dynamics (MD) simulations to capture the entire process by which several drugs bind to two archetypal GPCRs. Despite the fact that our simulations lacked any "knowledge" of the binding site, and thus required the drugs to spontaneously "discover" the binding pocket, they resulted in bound conformations that recapitulate crystallographic poses to subangstrom accuracy. These binding events occur on microsecond timescales that, until very recently, were beyond the reach of atomistic MD simulations.

Our results reveal not only the predominant pathway into the binding site, but also the energetic barriers that govern drug binding and unbinding kinetics. We found that drugs encounter two major barriers on the binding pathway: the "expected" barrier suggested by receptor geometry, proximal to the binding pocket, and also an unexpected, earlier barrier at the receptor surface. This early barrier coincides with, and appears to be tied to, substantial drug–receptor dehydration that occurs far from the binding pocket.

Results

We performed all-atom MD simulations in which four distinct ligands bound spontaneously to the β_2-adrenergic receptor (β_2AR): three antagonists (the "beta blocker" drugs propranolol and alprenolol, used to treat hypertension and angina pectoris, and dihydroalprenolol, a key experimental tool) and one agonist (isoproterenol, used to treat bradycardia and heart block). We also simulated the binding of dihydroalprenolol to the β_1-adrenergic receptor (β_1AR). We performed 82 simulations lasting from 1 to 19 μs each, resulting in a total of 21 spontaneous binding events (Tables S1 and S2).

All simulations were completely blind to the location of the binding site, and did not incorporate any artificial guiding or biasing forces. Ligands were initially positioned at least 30 Å from the binding pocket and 12 Å from the receptor surface. They diffused extensively about the receptor before entering the binding pocket (Fig. 1*A*); once bound, ligands remained bound for the remainder

Author contributions: R.O.D., A.C.P., D.H.A., D.W.B., and D.E.S. designed research; R.O.D., A.C.P., D.H.A., and H.X. performed research; Y.S. and H.X. conributed new reagents/analytic tools; R.O.D., A.C.P., D.H.A., D.W.B., and P.M. analyzed data; and R.O.D., A.C.P., D.H.A., D.W.B., and D.E.S. wrote the paper.

The authors declare no conflict of interest.

This article is a PNAS Direct Submission.

Freely available online through the PNAS open access option.

[1]R.O.D, A.C.P., and D.H.A. contributed equally to this work.

[2]To whom correspondence may be addressed. E-mail: Ron.Dror@DEShawResearch.com or David.Shaw@DEShawResearch.com.

This article contains supporting information online at www.pnas.org/lookup/suppl/doi:10.1073/pnas.1104614108/-/DCSupplemental.

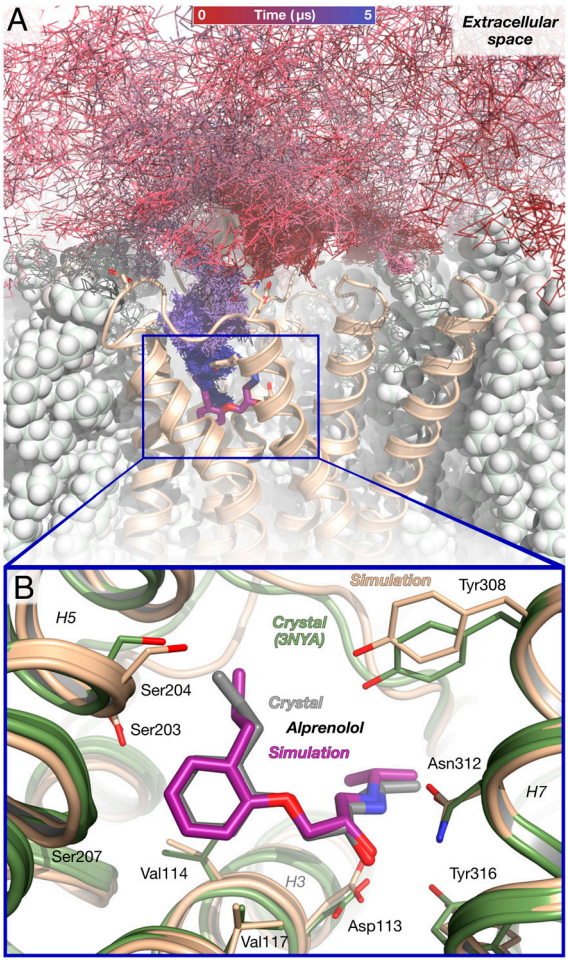

Fig. 1. Alprenolol binds spontaneously to β_2AR in unbiased molecular dynamics simulations, achieving the crystallographic pose. (*A*) The path taken by an alprenolol molecule as it diffuses about the receptor and then binds. The final, bound alprenolol is shown as a stick figure (purple carbon atoms); the protein as a tan cartoon; and the lipid bilayer as white spheres. (*B*) Close-up view of the simulated alprenolol pose shown in (*A*) superimposed on the alprenolol–β_2AR crystal structure (gray ligand, green cartoon; PDB entry 3NYA). Data from simulation 1 (Table S2).

of the simulation. Binding rates in simulation were comparable with experimentally observed rates: our simulations suggest an on-rate of 3.1×10^7 M^{-1} s^{-1} for alprenolol and dihydroalprenolol binding to β_2AR at 37 °C, close to the experimentally derived value of approximately 1.0×10^7 M^{-1} s^{-1} (19; see *SI Text*). Likewise, the dihydroalprenolol–β_2AR binding energy determined by free-energy perturbation calculations, -13.4 ± 1.6 kcal/mol, is within error of the experimentally derived value of -12.2 kcal/mol (20; see *SI Text*).

We describe first the binding of (*S*)-alprenolol and (*S*)-dihydroalprenolol to β_2AR (Fig. 2*A*). These ligands interact essentially identically with β-adrenergic receptors both in our simulations and in biochemical studies (20, 21); we refer to both ligands simply as "alprenolol" except where otherwise indicated. We then turn to the other ligands and β_1AR, noting extensive similarities in the binding mechanism.

Bound Pose Matches Crystal Structure. In 6 of the 12 simulations in which alprenolol bound to β_2AR, it adopted a pose matching the alprenolol-bound β_2AR crystal structure (Fig. 1*B*), with a 0.8-Å root-mean-squared deviation (rmsd) between the average simulation pose and the crystallographic pose (22; *SI Text*). Once adopted, this pose remained stable for the duration of these 6 simulations; more simulations ended with alprenolol in the crystallographic pose than in any other. The other 6 simulations were terminated with alprenolol in the binding pocket in one of two alternative, metastable poses (Fig. 2, poses 4′ and 4″). These alternative poses, which were also observed transiently in several simulations that ended in the crystallographic pose, are likely less energetically favorable binding poses that convert slowly (relative to the timescale of our simulations) to the crystallographic pose.

A Dominant Binding Pathway. Alprenolol bound to β_2AR along a single dominant pathway. In 11 of the 12 simulations in which alprenolol bound to β_2AR, it entered via a strikingly similar pathway, not only following the same spatial route but also pausing at common, metastable intermediate conformations. Alprenolol passed between extracellular loops 2 and 3 (ECL2/ECL3) and then through the crevice between ECL2 and transmembrane helices 5, 6, and 7 to reach the binding pocket (Fig. 2*A* and Movie S1). In the single remaining simulation, alprenolol instead entered between ECL2 and helices 2 and 7. In our simulations, as in experiments (23), the alprenolol hydrophobic group (i.e., the 2-allyl[propyl]-benzene) tended to partition into the lipid bilayer, remaining there for a majority of the simulation; despite this, alprenolol never entered the binding pocket from the lipid bilayer.

The dominant alprenolol binding pathway comprises two major steps. First, alprenolol associated with a surface region we term the "extracellular vestibule," which is enclosed by ECL2, ECL3, and helices 5–7. The alprenolol hydrophobic group bound to the extracellular vestibule surface, contacting hydrophobic surfaces of residues such as Tyr308$^{7.35}$, Phe193^{ECL2}, Ala200$^{5.39}$, His296$^{6.58}$, and Val297$^{6.59}$. [Superscripts refer to Ballesteros–Weinstein residue numbering (24)]. Alprenolol typically spent several hundred nanoseconds in the vestibule, where it assumed several distinct poses (Fig. 2*A*). In the most common (Fig. 2, pose 2), the alprenolol ammonium group formed a salt bridge with Asp300^{ECL3}. This pose was often followed, temporally, by a pose in which the ammonium bound instead to the backbone carbonyl oxygen atom of Asp192^{ECL2} (Fig. 2, pose 3).

Second, alprenolol moved from the extracellular vestibule into the binding pocket by squeezing through a narrow passage between ECL2 and helices 5, 6, and 7. In some binding events, alprenolol immediately adopted the crystallographically observed pose upon entering the binding pocket. In others, it transiently adopted one of several alternative poses (Fig. 2, poses 4, 4′, and 4″)—all of which possessed the alprenolol ammonium–Asp113$^{3.32}$ carboxylate salt bridge—before relaxing into the crystallographic pose (Fig. 2, pose 5). In the simulation trajectory illustrated in Fig. 2, for example, alprenolol initially bound with its aliphatic chain twisted near the beta-hydroxyl group (Fig. 2, pose 4; see also Fig. S1); after 2.6 μs in this pose, it relaxed into the crystallographic pose, allowing the beta-hydroxyl to form a hydrogen bond with Asn293$^{6.55}$.

The Primary Barrier to Binding Lies Far Outside the Binding Pocket. Our simulations indicate the presence of two major energetic barriers along the binding pathway, corresponding to the two steps described above (Fig. 3). As might be expected, one of these barriers coincides with the passage leading from the vestibule to the binding pocket, by far the narrowest point alprenolol encounters along the binding pathway (Fig. 3 *A* and *C*).

Surprisingly, however, we found that alprenolol traverses the highest barrier prior even to its entry into the extracellular vestibule. Data obtained from two distinct simulation approaches support this conclusion. First, analysis of the unbiased binding simulations described above, all of which were initiated with alprenolol far from the receptor surface, indicated that once the hydrophobic group of alprenolol moved from bulk solvent into the vicinity of the extracellular vestibule—that is, it moved across the gold surface shown in Fig. 3*A*—the alprenolol molecule was more likely to bind than to escape back into bulk solvent. It is

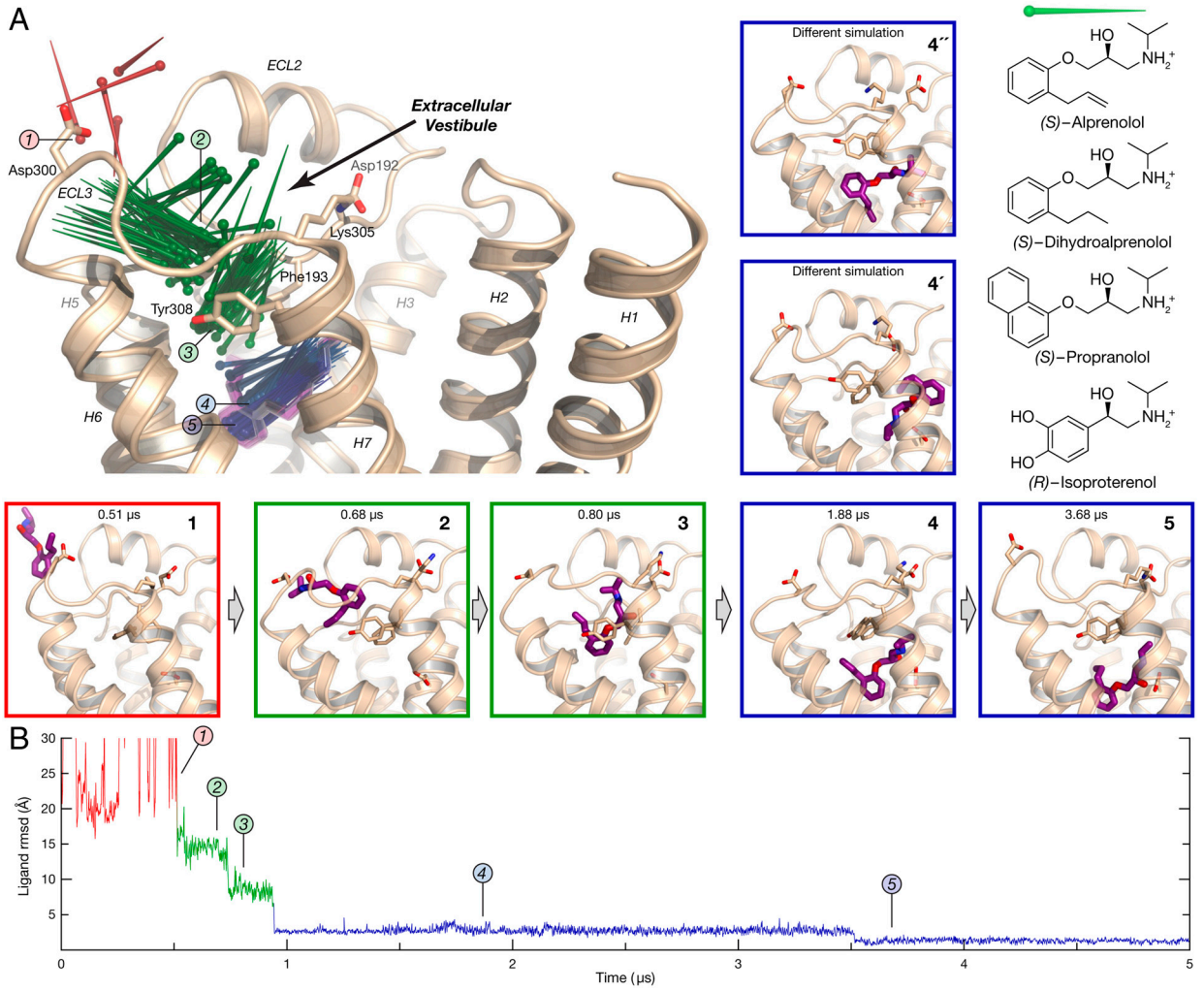

Fig. 2. The alprenolol–β_2AR binding pathway passes through several metastable states. (*A*) Pins indicate successive positions of an alprenolol molecule as it binds to β_2AR (the pin point is at the nitrogen atom position, and the round end is at the benzene ring center). Alprenolol moves from bulk solvent (red, pose 1), into the extracellular vestibule (green, poses 2 and 3), and finally into the binding pocket (blue, poses 4 and 5). Pose 5 matches the crystallographic pose (Fig. 1*B*), whereas pose 4 and two poses observed in a different simulation (4′ and 4′′) represent alternative, metastable poses in the binding pocket. The structures of ligands used in this study are shown at right. (*B*) Rmsd of alprenolol in simulation from the alprenolol-β_2AR crystal structure, calculated after aligning on protein binding pocket C_α atoms (*SI Text*). Poses 4′ and 4′′ from simulation 3; remaining data from simulation 1.

notable that this "50% binding probability" surface lies, for the most part, more than 15 Å away from the position of the alprenolol hydrophobic group in its (final) bound pose. Second, for each of four vestibule-bound alprenolol positions, two of which are shown in Fig. 3*A*, *Inset*, we initiated ten to twenty additional simulation trajectories, with random initial velocities. In each case, the ligand entered the binding pocket more frequently than it returned to bulk solvent. The relative frequency with which alprenolol molecules found in the extracellular vestibule proceed to bind or instead escape back into bulk solvent suggests that the energy difference between the two barriers is small, on the order of 1 kcal/mol. Both of these analyses independently support the conclusion that ligands in the metastable vestibule-bound state have already surmounted the highest barrier on the binding pathway.

Substantial Dehydration Accompanies Drug Entry into the Extracellular Vestibule. What accounts for the large barrier to alprenolol entry into the extracellular vestibule? Ligand entry into the vestibule does not require any noteworthy structural changes in the receptor or alprenolol itself (Fig. S1), and we found no electrostatic barrier to vestibule entry (Fig. S2). Yet experimental measurements have demonstrated that ligand–adrenergic receptor binding rates are well below diffusion-controlled rates, with correspondingly higher (enthalpic) barriers to binding (*SI Text*).

Our simulations suggest that this first barrier may be due instead to dehydration of both the drug and the extracellular vestibule as the drug enters the vestibule. High-affinity drug–receptor interactions are frequently stabilized by hydrophobic contacts that require substantial drug–receptor dehydration (25), and alprenolol–β_2AR is no exception. Alprenolol loses about 80% of its hydration shell as it binds to β_2AR. Significantly, the majority of ligand dehydration (63%; Fig. 3*D*) occurs as alprenolol enters the extracellular vestibule, far from the binding pocket. Ligand entry into the vestibule, which leads to substantial hydrophobic contacts and the burial of approximately 500 Å^2 of hydrophobic surface area (Table S3), coincides with the rapid evacuation of approximately 15 water molecules from the vestibule within 500–1000 ps (Fig. S3), a signature of a dewetting transition (14, 15, 26). This concerted motion of the ligand and multiple water molecules appears to represent a kinetic bottleneck to ligand entry into the extracellular vestibule.

The second energetic barrier, which alprenolol crosses as it moves from the extracellular vestibule into the binding pocket, involves structural changes from the receptor's crystallographic conformation (Fig. 3*C*), but also dehydration. As alprenolol

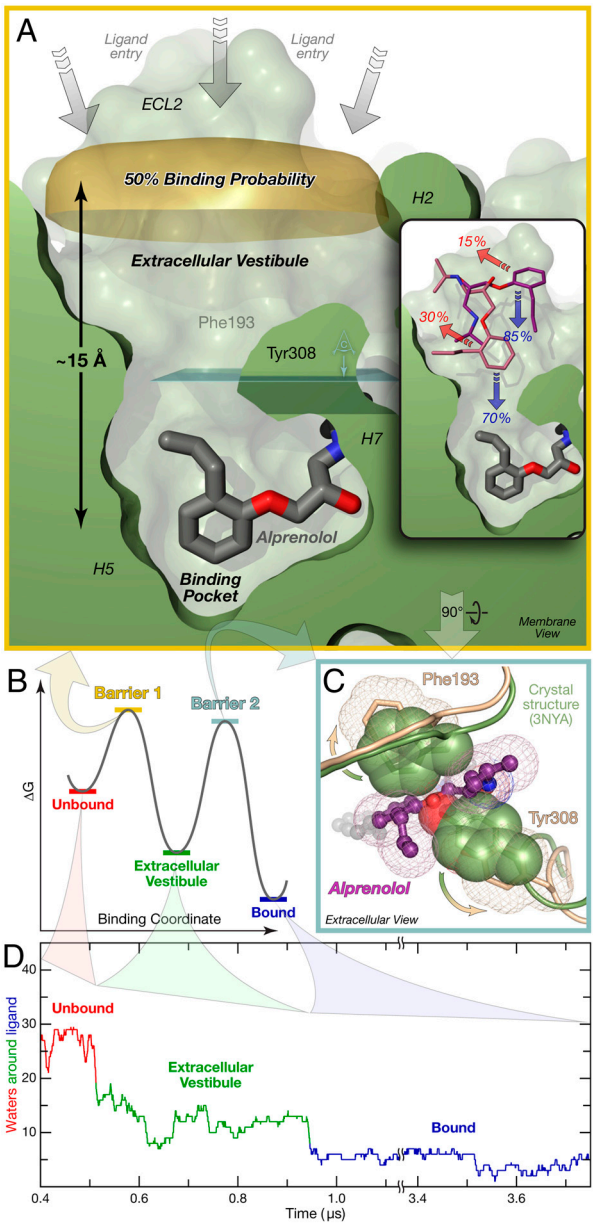

Fig. 3. Alprenolol must traverse two primary energetic barriers to bind to β_2AR. (*A*) The first and largest barrier precedes association with the extracellular vestibule. Alprenolol molecules for which the ring center has crossed the "50% binding probability" surface (from bulk solvent into the extracellular vestibule; above to below in this image) bind more often than they escape back into the bulk. (*Inset*) In repeated simulations initialized with alprenolol already in the vestibule, the ligand usually proceeded into the binding pocket. Binding/escape percentages are shown. (*B*) Schematic free-energy landscape for binding. (*C*) Phe193^{ECL2} and Tyr308$^{7.35}$ must separate for alprenolol to move from the extracellular vestibule into the binding pocket. View plane is indicated in light blue in (*A*). (*D*) Alprenolol loses more than half of its hydration shell as it enters the extracellular vestibule, and most of the rest as it enters the binding pocket (*SI Text*). Data from simulation 1.

passes into the binding pocket, Tyr308$^{7.35}$ and Phe193^{ECL2} separate enough for the ligand's hydrophobic group to pass between them, and the salt bridge between Asp192^{ECL2} and Lys305$^{7.32}$ breaks. These events, however, do not appear to be rate-limiting: while the ligand waits in the extracellular vestibule to enter the binding pocket, Tyr308$^{7.35}$ and Phe193^{ECL2} sometimes remain separated for over 200 ns, with the Asp192^{ECL2}–Lys305$^{7.32}$ salt bridge breaking and reforming hundreds of times during that period (Fig. S4). The rate may instead be limited, at least in part, by dehydration events: as the ligand enters the binding pocket, it loses the majority of its remaining hydration shell, and 50–60% of the water molecules in the binding pocket must also escape.

Similar Binding Pathways and Barriers for Other Drug–Receptor Pairs. We also simulated the binding of the beta blocker (*S*)-propranolol and the agonist (*R*)-isoproterenol to β_2AR. Propranolol adopted the expected pose, given those determined crystallographically for several structurally analogous antagonists (Fig. 4*A*) (22, 27). Isoproterenol entered the binding pocket and formed the expected salt bridge to Asp113$^{3.32}$, but it exhibited much more mobility than the antagonists when bound, likely reflecting the fact that the receptor remained in its inactive conformation, which has low agonist affinity. (Receptor activation takes place on millisecond timescales (28), several orders of magnitude longer than our simulations.)

Our simulations of propranolol and isoproterenol binding largely recapitulated our findings with alprenolol. These drugs generally followed the predominant alprenolol binding pathway, pausing in the extracellular vestibule before entering the binding pocket (Fig. 4*B*); one propranolol molecule followed the alternative alprenolol pathway. Although the smaller number of simulations and binding events (three events for propranolol and one for isoproterenol) prevents an accurate assessment of the relative barrier heights, the observed balance between escape from the vestibule into bulk solvent and progression to the binding pocket suggests that the two barriers are again of similar height. Like alprenolol, propranolol and isoproterenol lost approximately 60% of their hydration shells upon association with the extracellular vestibule; dewetting likely thus contributes to the vestibule entry barrier for these drugs as well.

Finally, we simulated the binding of dihydroalprenolol to β_1AR, achieving a bound pose that matched crystallographic data (Fig. S5*A* and refs. 22 and 29). The binding pathway was similar to that observed for β_2AR, with a metastable state in the extracellular vestibule and with substantial dewetting taking place upon ligand association with the vestibule (Fig. 4*B*). β_1AR lacks the extracellular salt bridge corresponding to Asp192^{ECL2}–Lys305$^{7.32}$ in β_2AR, however, allowing the β_1AR vestibule to extend further toward helix 2. In addition, one of the alternative binding poses, in which the dihydroalprenolol hydrophobic group interacts with helix 2 (Fig. S5*B*; see also Fig. 2, pose 4′), was observed more frequently with β_1AR than with β_2AR. Although this alternative pose is likely transient, a mutagenesis study has suggested that a pose with this orientation may represent an important binding mode for β_1AR antagonists under certain conditions (30).

Discussion

In the simulations of GPCR–drug binding we report here, diverse drugs bound to two β-adrenergic receptors and adopted crystallographically validated binding poses. Unlike standard docking approaches (31), which search for the best pose within a predefined binding site, our unbiased, atomistic MD simulations reproducibly identified and maintained the correct pose without user intervention or incorporation of any prior knowledge of the binding site. Furthermore, our approach naturally revealed the binding pathways and the energetic barriers encountered along those pathways, while taking into account the significant flexibility of both drugs and receptors. Our simulations also allowed determination of previously unknown binding sites, including transiently populated sites that might be targeted by allosteric modulators (Fig. 2*A* and Fig. S6). Direct simulation of the binding process thus provides access to information that is particularly difficult to obtain experimentally.

The Binding Pathway: Barriers, Kinetics, and Dewetting. The three beta blockers and the beta agonist we studied all bound to the receptors along a predominant pathway involving entry into

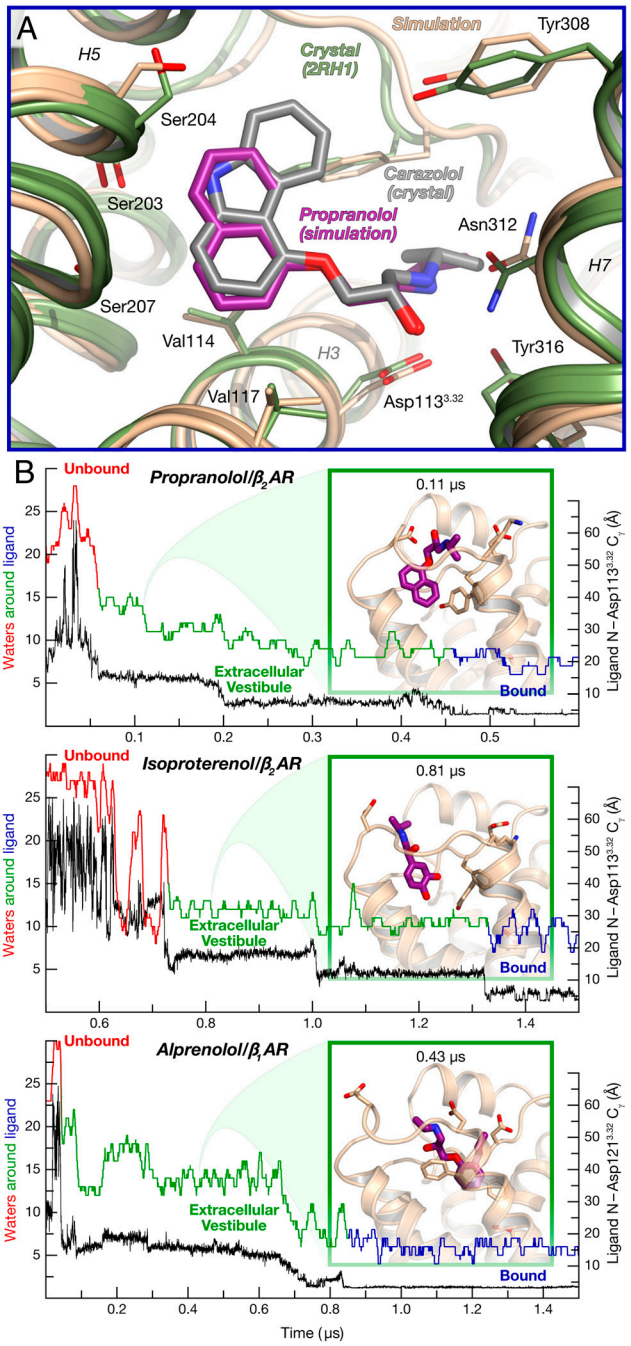

Fig. 4. Other drug–receptor pairs follow the same binding pathway. (*A*) Bound pose of propranolol (purple), superimposed on the carazolol–β_2AR crystal structure (PDB entry 2RH1, gray) (data from simulation 15). (*B*) Distance to binding pocket (ligand nitrogen atom to Asp$^{3.32}$ C_γ) and ligand hydration for propranolol and isoproterenol binding to β_2AR, and for alprenolol binding to β_1AR (data from simulations 13, 16, and 21). The insets illustrate a typical extracellular-vestibule-bound state for each simulation.

the extracellular vestibule, drug residence in the vestibule, and finally drug entry into the binding pocket, where the drug often took on one of several metastable poses before adopting the crystallographically observed conformation. Unexpectedly, the barrier to entry into the extracellular vestibule was comparable to —and, at least in the case of alprenolol binding to β_2AR, higher than—the barrier for entry into the binding pocket, even though the latter required traversal of a narrow passage with accompanying deformation of the receptor structure. The barrier to entry into the extracellular vestibule is associated with surprisingly large dehydration of both drug and receptor that takes place as the drug associates with the vestibule.

Our simulations of drug binding also illuminate the process of unbinding: in the absence of external driving forces, the unbinding process is the reverse of the binding process, following the same pathway and traversing the same barriers in the opposite order. Thus, as alprenolol unbinds, it first moves from the binding pocket into the extracellular vestibule, passing between Tyr308$^{7.35}$ and Phe193^{ECL2} (Fig. 3*B*, "Barrier 2"), and then exits from the vestibule into the bulk solvent as water enters the vestibule in a concerted fashion (Fig. 3*B*, "Barrier 1"). In a recent computational study, carazolol was observed to exit the β_2AR binding pocket along many routes, with the extracellular vestibule route ranking second (8); this difference from our results might be due to the choice of ligand, but more likely it reflects the forces applied in that study to evict carazolol from the binding pocket within a few nanoseconds, a time period about 14 orders of magnitude shorter than its experimental dissociation half-life (32).

By characterizing the binding pathway and the major energetic barriers along it, our results provide a foundation for the rational optimization of drug binding and unbinding kinetics, which are now recognized to play a critical role in drug efficacy, selectivity, and safety (3, 4). Because the two barriers are of similar height, changes to either can substantially affect binding and unbinding rates. Geometric factors, such as ligand size and flexibility, will likely affect the barrier to binding pocket entry more than the barrier to vestibule entry. Ligand hydrophobicity and other factors associated with dehydration may, however, contribute as much to both barriers—particularly the vestibule entry barrier—as geometry and electrostatics.

The dehydration observed early on the binding pathway, and its connection to a major kinetic barrier, is particularly intriguing given the widely recognized importance of ligand and binding-site dehydration in drug–receptor affinity. Greater drug hydrophobicity usually leads to greater affinity, because changes in water structure upon drug binding—in particular, the increased disorder of water molecules released from the binding pocket—often dominate the binding free energy and thus make the largest contribution to affinity (25). Our results suggest that this dehydration, and the points on the binding pathway at which it takes place, play an important role in determining binding kinetics as well as affinity.

Beyond providing insight into elements of the binding process that have proven difficult to probe experimentally, our simulation results also suggest avenues for future experimental investigation. Free-energy perturbation calculations indicate that dihydroalprenolol binds to the β_2AR extracellular vestibule—the main intermediate we observe prior to ligand entry into the orthosteric binding pocket—with a K_D of about 5 μM (*SI Text*). Crystal structures determined with modified beta blockers, in which the ether oxygen atom is substituted by selenium, may thus reveal anomalous scattering density peaks in the vestibule. Similarly, the [^{19}F]-NMR chemical shift of a semisynthetic β_2AR in which a vestibule hydrophobic residue is substituted by Cys-SCH_2CF_3 should be very sensitive to the binding there of aromatic ligands. Blockade of the orthosteric site, by mutation or by presaturation with a slowly dissociating beta blocker, may even render ligand binding in the vestibule detectable by conventional means such as a radioligand binding assay. By contrast, incorporation of sufficiently large residues in the extracellular vestibule could block the dominant binding pathway, slowing ligand association with and dissociation from the orthosteric binding pocket.

Further investigation, perhaps using computational techniques similar to those demonstrated here, will be necessary to determine the similarities and differences in the pathways, energetics, and kinetics of ligand binding to different receptors. Detailed binding pathways likely vary among GPCRs, and perhaps even for a given GPCR in different conformational states. Several stu-

dies have also suggested that highly hydrophobic ligands may enter and leave certain GPCRs directly through the lipid bilayer (9, 10). Nevertheless, the conserved architecture of the GPCR family, with the binding pocket buried deep within a seven transmembrane helix bundle, suggests that many GPCRs likely share similar binding pathways. Moreover, characteristics of the binding process we have observed here for β-adrenergic receptors, including the presence of a major energetic barrier at the point where the drug first associates with the receptor surface and its connection to early drug–receptor dehydration, may even apply beyond the GPCR family, particularly to other receptors with deep, well-defined binding pockets.

Implications for Allosteric Modulation. Allosteric GPCR modulators, which bind at sites distinct from the classical orthosteric binding pocket, hold the promise of enhanced selectivity compared to orthosteric GPCR drugs (33). The design of allosteric drugs has been hindered, however, by a lack of structural information. Although the orthosteric site was the dominant binding site observed in our simulations—and the only site to which ligands remained stably bound—we also observed several previously unknown, metastable binding sites (Fig. 2*A* and Fig. S6). Unbiased simulations of ligand binding, such as those presented here, may thus provide a means to identify the binding sites of known allosteric modulators and to discover potential binding sites for novel allosteric modulators.

Metastable drug binding to the extracellular vestibule (Fig. 2*A*) is of particular interest in light of experimental data for the binding of allosteric modulators to muscarinic acetylcholine receptors. Binding of gallamine and related compounds to these receptors dramatically slows the association and dissociation of orthosteric ligands (34). Mutagenesis data indicate that residues in ECL2 and near the ECL3/helix 7 junction are involved in gallamine binding (18). We speculate that gallamine binds in the extracellular vestibule. By "getting stuck" at this intermediate point on the dominant binding pathway, gallamine would directly block access to, or egress from, the orthosteric binding pocket. Recent data suggests that orthosteric ligands can bind weakly in the same position as gallamine (35), as would be expected if the gallamine binding site represents a metastable point on the binding pathway of orthosteric ligands.

As additional GPCR structures become available and as advances in computer technology enable ever longer simulations, the approach presented here will become applicable to more receptors and ligands. Such simulations promise to complement traditional experimental measurements by providing an atomic-level description of the binding process for orthosteric and allosteric GPCR modulators, including the binding pathway and the energetic barriers that control binding kinetics, both when the binding site is known in advance and when it is not.

Methods

We performed molecular dynamics simulations of β_1AR and β_2AR, with lipids and water represented explicitly, using the CHARMM force field (36) on Anton (37), a special-purpose machine that accelerates such simulations by orders of magnitude. Each simulation began with the receptor in the crystallographic conformation [Protein Data Bank (PDB) ID entries 2VT4 for β_1AR (29) and 2RH1 for β_2AR (27)], but with the cocrystallized antagonist (cyanopindolol or carazolol) removed. Ten identical ligand molecules were placed in the bulk solvent surrounding the receptor. No artificial forces were applied to the ligands, which diffused throughout the simulated water and lipids. Further details are provided in *SI Text*.

ACKNOWLEDGMENTS. We thank Brian Kobilka and Michael Bokoch for questions and comments that inspired this work; Woody Sherman for suggesting the study of binding kinetics; Kresten Lindorff-Larsen, Stefano Piana, Kim Palmo, and Morten Jensen for helpful advice; Ansgar Philippsen for creating the movie; Bruce Berne for comments on the manuscript; and Rebecca Kastleman and Mollie Kirk for editorial assistance.

1. Weiland GA, Minneman KP, Molinoff PB (1979) Fundamental difference between the molecular interactions of agonists and antagonists with the β-adrenergic receptor. *Nature* 281:114–117.
2. Ward WH, Holdgate GA (2001) Isothermal titration calorimetry in drug discovery. *Prog Med Chem* 38:309–376.
3. Lu H, Tonge PJ (2010) Drug-target residence time: Critical information for lead optimization. *Curr Opin Struct Biol* 14:467–474.
4. Swinney DC (2008) Applications of binding kinetics to drug discovery: Translation of binding mechanisms to clinically differentiated therapeutic responses. *Pharmaceut Med* 22:23–34.
5. Baldwin AJ, Kay LE (2009) NMR spectroscopy brings invisible protein states into focus. *Nat Chem Biol* 5:808–814.
6. Hargrove MS (2005) Ligand binding with stopped-flow rapid mixing. *Methods Mol Biol* 305:323–342.
7. Westenhoff S, et al. (2010) Time-resolved structural studies of protein reaction dynamics: A smorgasbord of X-ray approaches. *Acta Crystallogr A* 66:207–219.
8. Wang T, Duan Y (2009) Ligand entry and exit pathways in the β_2-adrenergic receptor. *J Mol Biol* 392:1102–1115.
9. Hildebrand PW, et al. (2009) A ligand channel through the G protein coupled receptor opsin. *PLoS One* 4:e4382.
10. Hurst DP, et al. (2010) A lipid pathway for ligand binding is necessary for a cannabinoid G-protein-coupled receptor. *J Biol Chem* 285:17954–17964.
11. Wang Y, Tajkhorshid E (2008) Electrostatic funneling of substrate in mitochondrial inner membrane carriers. *Proc Natl Acad Sci USA* 105:9598–9603.
12. Sharp K, Fine R, Honig B (1987) Computer simulations of the diffusion of a substrate to an active site of an enzyme. *Science* 236:1460–1463.
13. Grubmüller H, Heymann B, Tavan P (1996) Ligand binding: molecular mechanics calculation of the streptavidin-biotin rupture force. *Science* 271:997–999.
14. Setny P, et al. (2009) Dewetting-controlled binding of ligands to hydrophobic pockets. *Phys Rev Lett* 103:187801.
15. Ahmad M, Gu W, Helms V (2008) Mechanism of fast peptide recognition by SH3 domains. *Angew Chem Int Ed Engl* 47:7626–7630.
16. Shan Y, et al. (2011) How does a drug molecule find its target binding site? *J Am Chem Soc* 133:9181–9183.
17. Rosenbaum DM, Rasmussen SG, Kobilka BK (2009) The structure and function of G-protein-coupled receptors. *Nature* 459:356–363.
18. May LT, Leach K, Sexton PM, Christopoulos A (2007) Allosteric modulation of G-protein-coupled receptors. *Annu Rev Pharmacol Toxicol* 47:1–51.
19. Limbird LE, Lefkowitz RJ (1976) Negative cooperativity among β-adrenergic receptors. *J Biol Chem* 251:5007–5014.
20. Caron MG, Lefkowitz RJ (1976) Solubilization and characterization of the β-adrenergic receptor binding sites of frog erythrocytes. *J Biol Chem* 251:2374–2384.
21. Alexander RW, Williams LT, Lefkowitz RJ (1975) Identification of cardiac β-adrenergic receptors by (–) [^{3}H]alprenolol binding. *Proc Natl Acad Sci USA* 72:1564–1568.
22. Wacker D, et al. (2010) Conserved binding mode of human β_2 adrenergic receptor inverse agonists and antagonist revealed by X-ray crystallography. *J Am Chem Soc* 132:11443–11445.
23. Dax EM, Partilla JS (1982) Adrenergic ligand liposolubility in membranes: Direct assessment in a *beta*-adrenergic binding system. *Mol Pharmacol* 22:5–7.
24. Ballesteros JA, Weinstein H (1995) Integrated methods for the construction of three dimensional models and computational probing of structure function relations in G-protein-coupled receptors. *Methods Neurosci* 25:366–428.
25. Böhm H-J, Klebe G (1996) What can we learn from molecular recognition in protein–ligand complexes for the design of new drugs? *Angew Chem Int Ed Engl* 35:2588–2614.
26. Liu P, Huang X, Zhou R, Berne BJ (2005) Observation of a dewetting transition in the collapse of the melittin tetramer. *Nature* 437:159–162.
27. Cherezov V, et al. (2007) High-resolution crystal structure of an engineered human β_2-adrenergic G-protein-coupled receptor. *Science* 318:1258–1265.
28. Vilardaga J-P, Bünemann M, Krasel C, Castro M, Lohse MJ (2003) Measurement of the millisecond activation switch of G-protein-coupled receptors in living cells. *Nat Biotechnol* 21:807–812.
29. Warne T, et al. (2008) Structure of a β_1-adrenergic G-protein-coupled receptor. *Nature* 454:486–491.
30. Rezmann-Vitti LA, et al. (2004) Site-directed mutagenesis of the rat β_1-adrenoceptor. Involvement of Tyr$^{356(7.43)}$ in (+/–)cyanopindolol but not (+/–)[^{125}Iodo]cyanopindolol binding. *Eur J Med Chem* 39:625–631.
31. Kolb P, et al. (2009) Structure-based discovery of β_2-adrenergic receptor ligands. *Proc Natl Acad Sci USA* 106:6843–6848.
32. Rosenbaum DM, et al. (2007) GPCR engineering yields high-resolution structural insights into β_2-adrenergic receptor function. *Science* 318:1266–1273.
33. Conn PJ, Christopoulos A, Lindsley CW (2009) Allosteric modulators of GPCRs: A novel approach for the treatment of CNS disorders. *Nat Rev Drug Discov* 8:41–54.
34. Stockton JM, Birdsall NJM, Burgen ASV, Hulme EC (1983) Modification of the binding properties of muscarinic receptors by gallamine. *Mol Pharmacol* 23:551–557.
35. Redka DS, Pisterzi LF, Wells JW (2008) Binding of orthosteric ligands to the allosteric site of the M_2 muscarinic cholinergic receptor. *Mol Pharmacol* 74:834–843.
36. MacKerell AD, Jr, et al. (1998) All-atom empirical potential for molecular modeling and dynamics studies of proteins. *J Phys Chem B* 102:3586–3616.
37. Shaw DE, et al. (2009) Millisecond-scale molecular dynamics simulations on Anton. *Proceedings of the Conference on High Performance Computing, Networking, Storage and Analysis (SC09)* (ACM, New York).

Supporting Information

Dror et al. 10.1073/pnas.1104614108

SI Methods

Methods for Molecular Dynamics Simulations. In all simulations, the receptor was embedded in a hydrated lipid bilayer with all atoms, including those in the lipids and water, represented explicitly. Production simulations were performed on Anton (1), a special-purpose computer designed to accelerate standard molecular dynamics simulations by orders of magnitude. Prior to production simulation, systems were equilibrated using Desmond (2) on a commodity cluster, according to the protocol described below.

System Setup and Simulation Protocol. Simulations of β_2AR were based on the crystal structure of the carazolol-β_2AR complex [Protein Data Bank (PDB) entry 2RH1], and simulations of β_1AR were based on the structure of the cyanopindolol-β_1AR complex (PDB ID entry 2VT4, chain B). The β_2AR crystal structure was determined using a β_2AR-T4 lysozyme (T4L) fusion protein, in which intracellular loop 3 (ICL3) of the receptor was replaced by T4L; the T4L was omitted in our simulations of β_2AR. The crystal structure of β_1AR was determined using a construct with six thermostabilizing point mutations and a deletion of most of ICL3; we back-mutated the six-point mutations to their wild-type residues using Maestro (Schrödinger LLC), but the ICL3 deletion was left unchanged. All chain termini were capped with neutral groups (acetyl and methylamide). The cocrystallized ligands carazolol and cyanopindolol were deleted. Hydrogens were added to the crystal structures using Maestro, as described in previous work (3). All titratable residues were left in the dominant protonation state at pH 7.0, except for Glu122$^{3.41}$ and Asp79$^{2.50}$ in β_2AR and Glu130$^{3.41}$ and Asp87$^{2.50}$ in β_1AR, which were protonated. Asp79$^{2.50}$ and Asp87$^{2.50}$ correspond to rhodopsin Asp83$^{2.50}$, which is protonated during the entire photocycle (4). Glu122$^{3.41}$ and Glu130$^{3.41}$ face the lipid bilayer and thus are likely protonated (3); in addition, a similarly positioned residue in rhodopsin (Glu122$^{3.37}$) is protonated during the entire photocycle (4).

Prepared protein structures were inserted into an equilibrated palmitoyl oleoyl phosphatidyl choline (POPC) bilayer as described in previous work (5), and 10 ligands were placed at arbitrary positions in the aqueous phase, each at least 30 Å away from the binding pocket of the receptor. Chloride ions were added to neutralize the net charge of the system. Simulations of β_2AR under conditions A, C, D, and E (Table S1) initially measured $83 \times 71 \times 87$ Å^3 and contained 131 lipid molecules, 9,706 water molecules, and 14 chloride ions, for a total of approximately 52,000 atoms. Simulations of β_2AR under condition B (Table S1), which had approximately 100 mM NaCl added to the aqueous phase (in addition to the ions present in the previous condition), initially measured $83 \times 83 \times 87$ Å^3 and contained 160 lipid molecules, 11,314 water molecules, 20 sodium ions, and 34 chloride ions, for a total of approximately 60,000 atoms. Simulations of β_1AR (condition F) initially measured $76 \times 77 \times 86$ Å^3 and contained 136 lipid molecules, 9,523 water molecules, 1 sodium ion (from the crystal structure), and 19 chloride ions, for a total of approximately 52,000 atoms. The higher NaCl concentration did not appear to affect the binding pathway.

One system for each of the six conditions was equilibrated using Desmond in the NPT ensemble at 310 K (37 °C) and 1 bar using the Berendsen coupling scheme with 5 kcal mol^{-1} Å^{-2} harmonic-position restraints applied to all non-hydrogen atoms of the protein and ligands; these restraints were tapered off linearly over 5 ns. Unrestrained systems were then simulated for an additional 5 ns to further equilibrate the aspect ratio of the simulation box. During the equilibration process, van der Waals and short-range electrostatic interactions were cut off at 9 Å and long-range electrostatic interactions were computed using the Particle Mesh Ewald method (6) with a $64 \times 64 \times 64$ grid, $\sigma = 2.26$ Å, and fifth-order B-splines for interpolation. All bond lengths to hydrogen atoms were constrained using M-SHAKE (7). A RESPA integrator (8) was used with a time step of 2 fs, and long-range electrostatics were computed every 6 fs.

Production simulations on Anton were initiated from the final snapshot of the corresponding equilibration runs on Desmond, with velocities sampled from the Boltzmann distribution at 310 K, using the same integration scheme, temperature, and pressure. Van der Waals and short-range electrostatic interactions were cut off at 13.5 Å, and long-range electrostatics were computed using the k-space Gaussian Split Ewald method (9) with a $32 \times 32 \times 32$ grid, $\sigma = 3.33$ Å, and $\sigma_s = 2.35$ Å.

Force Field Parameters. The CHARMM27 (10) parameter set with CMAP terms (11) and a recently introduced correction to charged side-chain electrostatics (12) was used for all protein molecules and salt ions in conjunction with the CHARMM TIP3P (13) water model and a modified CHARMM lipid force field (14). Force field parameters for palmitoyl-cysteine were designed previously (3). Force field parameters for dihydroalprenolol, alprenolol, propranolol, and isoproterenol were transferred from aryloxypropanolamine parameter sets previously designed for carazolol (3), and parameters for the alprenolol allyl group were transferred from the model compound 1,4-pentadiene from the CHARMM General Force Field (15). All ligands were simulated in their protonated (ammonium) state. Full parameter sets are available upon request.

Analysis Protocols. Trajectory snapshots, each containing a record of all atom positions at a particular instant in time, were saved every 180 ps during production simulations. Portions of some trajectories were later recomputed to obtain snapshots every 1 ps. Distance and rmsd measurements were computed using the HiMach parallel analysis framework (16).

Ligand rmsd was calculated for the heavy atoms of the ligand after aligning the protein C_α atoms near the binding site (β_2AR residues 109, 110, 113, 114, 117, 118, 193, 203, 207, 286, 289, 290, 293, 312, and 316) to the corresponding atoms in the alprenolol–β_2AR crystal structure. Water traces in Fig. 3 and Fig. 4 were smoothed with a centered 9 ns median filter.

VMD (17) was used to visualize trajectories and to produce Fig. S6; other molecular images were rendered using PyMol (18) and POV-Ray (Persistence of Vision Pty. Ltd.; http://www.povray.org).

Estimating the β_2AR–Alprenolol On-Rate from Simulation. To estimate the k_{on} of β_2AR–alprenolol binding from our simulations, we pooled all 50 simulations under conditions A–C of Table S1 (that is, all simulations involving β_2AR and either alprenolol or dihydroalprenolol, including those where no binding took place; we also calculated such estimates separately for dihydroalprenolol [conditions A–B] and alprenolol [condition C], leading to similar results).

Calculating k_{on} directly is complicated by the fact that the ligand concentration in the aqueous phase of our simulations changes over time; the ligands rapidly partition into the bilayer, and subsequently spend only approximately 2% of their time in the aqueous phase. Because ligands only bind to the receptor via

the aqueous phase, the effective total amount of time during which a ligand has the opportunity to bind to the receptor, T_{eff}, is the total amount of time it spends in the aqueous phase before any ligand has already bound to the receptor. Assuming pseudo-first-order binding kinetics, binding events can be modeled as a Poisson process sampled over an interval of length T_{eff}. Aggregating across the 30 simulations under conditions A and C (which include 9,706 water molecules and 10 ligands) gives $T_{\text{eff,AC}} = 44.1$ μs (total, summed across all ligands). Aggregating across the 20 simulations under condition B (which include 11,314 water molecules and 10 ligands) gives $T_{\text{eff,B}} = 27.6$ μs. A total of 12 binding events were observed in these simulations. The maximum likelihood estimate of the rate of a Poisson process is the number of observed events divided by the time period of observation. For a given number of ligands, the ligand concentration, and thus the rate of the Poisson process under observation, will scale inversely with the number of water molecules in the system. Taking into account the different numbers of water molecules under the different simulation conditions, the maximum likelihood estimate for k_{on} evaluates to 3.1×10^7 $\text{M}^{-1}\,\text{s}^{-1}$ at 37 °C.

Limbird and Lefkowitz (19) measured $k_{\text{off}} \approx 4.3 \times 10^{-3}$ s^{-1} at 37 °C, and presented additional data indicating that $K_D \approx 0.45$ nM under the same conditions. Together, these two values indicate that $k_{\text{on}} \approx 1.0 \times 10^7$ $\text{M}^{-1}\,\text{s}^{-1}$. Contreras et al. (20) measured the association rate directly at a lower temperature (25 °C), obtaining $k_{\text{on}} \approx 3.8 \times 10^6$ $\text{M}^{-1}\,\text{s}^{-1}$.

Calculation of 50% Binding Probability Surface. To compute the "50% binding probability" surface shown in Fig. 3*A*, we performed a trajectory commitment analysis based on all simulations under conditions A–C (Table S1), all of which were initiated with alprenolol far from the receptor surface. All trajectory snapshots were aligned by superimposing the C_α atoms of the transmembrane portions of the seven helices (residues 32–56, 70–94, 106–129, 150–170, 197–220, 275–295, and 307–325), thus establishing a coordinate system relative to the receptor. In this coordinate system, a spatial $16 \times 16 \times 16$ grid of 2-Å voxels was defined over a volume enclosing the extracellular surface of the receptor and the binding pocket. An alprenolol molecule in a simulation was defined as bound to the orthosteric site once its ammonium nitrogen atom sampled a position within 0.5 Å of the position of the alprenolol ammonium nitrogen atom in the aligned crystal structure (PDB entry 3NYA). For each alprenolol molecule in all simulations of β_2AR, an attempt was recorded each time the molecule entered the grid and subsequently exited the grid or went on to bind to the orthosteric site. The voxels visited by the alprenolol ring center on each attempt were identified, and the committor function for binding—the probability that an alprenolol molecule would go on to bind to the orthosteric site before leaving the grid—was estimated for each voxel as the fraction of attempts passing through that voxel that resulted in binding. The resulting spatial committor function maps were smoothed using a 1.5-Å Gaussian blur for visualization purposes (in particular, to compute the 50% binding probability surface).

Calculation of Binding Probabilities Associated with Particular Snapshots. We computed the binding probabilities associated with each of 5 snapshots chosen from simulation 1 (Table S2) by initializing either 10 or 20 additional simulations from each of these snapshots. For each of these additional simulations, all atom positions corresponded to those of the chosen snapshot, but random velocities for each atom were drawn from a Boltzmann distribution. The lengths of these additional trajectories were mostly on the order of 1 μs, although some were as long as 6 μs, giving a total additional simulation time of 113 μs. The binding probability (or committor value) for each snapshot was computed as the fraction of simulations initiated from that snapshot in which the ligand entered the binding pocket before it escaped into bulk solvent. Of the five chosen snapshots, alprenolol was within the extracellular vestibule in four (resulting in binding probabilities of 0.55, 0.70, 0.70, and 0.85) and slightly outside the vestibule in one (resulting in a binding probability of 0.2).

Experimental Data on the Energetic Barrier to Binding. The experimentally determined rate of alprenolol binding to β_2AR ($k_{\text{on}} \approx 1.0 \times 10^7$ $\text{M}^{-1}\,\text{s}^{-1}$ at 37 °C; see "Estimating the β_2AR-alprenolol on-rate from simulation," above) suggests that the process is not diffusion-controlled, as this rate is about two orders of magnitude slower than those typical of diffusion-controlled ligand binding [e.g., $k_{\text{on}} \approx 1.7 \times 10^9$ $\text{M}^{-1}\,\text{s}^{-1}$ for NADH binding to lactate dehydrogenase at 20 °C (21), and $k_{\text{on}} \approx 1 \times 10^9$ $\text{M}^{-1}\,\text{s}^{-1}$ for *N*-methylacridinium binding to acetylcholinesterase at 25 °C (22)].

Further support for this conclusion comes from an estimate of the enthalpic barrier to alprenolol–β_2AR binding based on experimental measurements of the binding free energy (or equivalently, the equilibrium dissociation constant, K_D) and the dissociation kinetics. First, the free energy of alprenolol–β_2AR binding, $\Delta G^\circ = -RT \ln K_D \approx -12.2$ kcal/mol (at 37 °C; 23), sets ΔG° for the bound and unbound ($\Delta G^\circ \equiv 0$) states. In fact, the equilibrium binding free energies of alprenolol and dihydroalprenol to β_1AR and β_2AR are all essentially identical (23–25). These ΔG° values, and the corresponding enthalpy and entropy values determined by van't Hoff analysis for dihydroalprenolol–β_1AR binding ($\Delta H^\circ = -3.5$ kcal/mol, $-T\Delta S^\circ = -8.8$ kcal/mol; 24), are consistent with those determined for structurally diverse beta blockers binding to β_1AR (26). Second, dihydroalprenolol dissociation from β_2AR is reported to exhibit an activation energy of $\Delta E^{\ddagger}_{\text{dissoc}} = +20.9$ kcal/mol (19); i.e., $\Delta H^{\ddagger}_{\text{dissoc}} = \Delta E^{\ddagger}_{\text{dissoc}} - RT = +20.3$ kcal/mol (37 °C). The activation enthalpy of alprenolol association is thus $\Delta H^{\ddagger}_{\text{assoc}} = \Delta H^\circ + \Delta H^{\ddagger}_{\text{dissoc}} = +16.8$ kcal/mol. This $\Delta H^{\ddagger}_{\text{assoc}}$ barrier (of ~15–20 kcal/mol) is much larger than the apparent enthalpy barriers observed for water self-diffusion ($\Delta E^{\ddagger} = +4.4$ kcal/mol [$\Delta H^{\ddagger} \approx +3.8$ kcal/mol]; 27) or the diffusion of (large or small) ligands in water ($\Delta E^{\ddagger} = +4$ to $+5$ kcal/mol [$\Delta H^{\ddagger} = +3$ to $+5$ kcal/mol]; 28), indicating that the binding of alprenolol to β_2AR is not diffusion-controlled.

We also performed an Eyring analysis of the same experimental data (19) that suggests (with less confidence, given uncertainty regarding various underlying assumptions) that $\Delta H^{\ddagger}_{\text{dissoc}} = +18.7$ kcal/mol, and $-T\Delta S^{\ddagger}_{\text{dissoc}} = +2.7$ kcal/mol. $\Delta G^{\ddagger}_{\text{dissoc}} = \Delta H^{\ddagger}_{\text{dissoc}} - T\Delta S^{\ddagger}_{\text{dissoc}} = +21.4$ kcal/mol, and thus $\Delta G^{\ddagger}_{\text{assoc}} = \Delta G^\circ + \Delta G^{\ddagger}_{\text{dissoc}} = +9.2$ kcal/mol. Incorporating ΔH° and $-T\Delta S^\circ$ further suggests that the enthalpy component of the association barrier is $\Delta H^{\ddagger}_{\text{assoc}} = \Delta H^\circ + \Delta H^{\ddagger}_{\text{dissoc}} = +15.2$ kcal/mol, in reasonable agreement with the +16.8 kcal/mol derived above. Similarly, the entropy component of the association barrier is $-T\Delta S^{\ddagger}_{\text{assoc}} = -T\Delta S^\circ - T\Delta S^{\ddagger}_{\text{dissoc}} = -6.1$ kcal/mol. This entropy gain ($T\Delta S^{\ddagger}_{\text{assoc}} \approx 5$–10 kcal/mol) linked with the association barrier is suggestive of the release of water from hydrophobic surfaces making a contribution to the association barrier, much as the entropy gain linked with the overall binding process ($T\Delta S^\circ = +8.8$ kcal/mol) is suggestive of the release of water making a contribution to ligand affinity.

Binding Free Energy Calculation. As an additional check of force field accuracy, we computed the dihydroalprenolol–β_2AR binding free energy through simulation using a free-energy perturbation method. The result, -13.4 ± 1.6 kcal/mol, is within error of the value of −12.2 kcal/mol calculated from the experimentally determined K_D of 2.2 nM at 37 °C (throughout, we assume a standard state of 1 M concentration) (29).

The free energy of dihydroalprenolol–β_2AR binding, $\Delta G_{\text{binding}}$, was computed by the double annihilation method (30),

in which $\Delta G_{\text{binding}}$ is computed as the free-energy difference between transfer of the ligand from vacuum into the receptor binding pocket and transfer of the same ligand from vacuum into aqueous solution. The binding pose of the ligand was taken from a snapshot in the simulation of dihydroalprenolol binding to β_2AR, which closely matches the ligand binding pose in the alprenolol–β_2AR complex crystal structure (PDB entry 3NYA); the rmsd of the dihydroalprenolol in that snapshot from its crystallographic position is 0.6 Å. In computing each transfer free energy, Lennard–Jones (LJ) interactions between the ligand and the rest of the system were modeled using a softcore potential (31)

$$V_{\text{softcore}}(r) = 4\epsilon\lambda\left[\left(\frac{1}{\alpha(1-\lambda)^2 + r^6/\sigma^6}\right)^2 - \frac{1}{\alpha(1-\lambda)^2 + r^6/\sigma^6}\right],$$

where $\alpha = 0.5$ and λ is an adjustable parameter; charges on the ligand atoms were scaled by a parameter λ_q. The free-energy difference between the system with $\lambda = 0$, $\lambda_q = 0$ and the system with $\lambda = 1$, $\lambda_q = 1$ are computed for both the ligand in the receptor's binding pocket, ΔG_{pocket}, and the ligand in the aqueous solution, $\Delta G_{\text{solution}}$; the difference between these two values, $\Delta G_{\text{pocket}} - \Delta G_{\text{solution}}$, corresponds to the free energy of binding. As is common in free-energy calculations, a number of intermediate stages with either (*i*) $0 \le \lambda \le 1$ and $\lambda_q = 0$, or (*ii*) $\lambda = 1$ and $0 \le \lambda_q \le 1$, were introduced to achieve better convergence. In simulating the ligand in the receptor at intermediates with $\lambda < 1$, artificial restraints were added to prevent the ligand from wandering away from the binding pocket; the contribution of these restraints to the free energy was corrected using a closed form (30). To achieve better convergence of the free-energy estimate, a few auxiliary intermediates were introduced with $\lambda = 0$, in which the torsional energies, the LJ repulsive energies, and the electric charges of the ligand and the receptor atoms in the ligand's vicinity were scaled down, to better sample the ligand and binding pocket conformations. Intermediates were chosen so as to minimize the statistical errors in the estimated free energies, following a previously outlined procedure (23). All the selected intermediates were simulated in parallel in a replica-exchange simulation, with exchanges between adjacent intermediates attempted every 1 ps. The simulations of the ligand in the receptor were run in Desmond in a constant surface tension ensemble (32) with temperature 310 K, normal pressure of 1 bar, and bilayer surface tension of 0 for about 50 ns per replica; the simulations of the ligand in the aqueous solution were run for 10 ns per replica. The free-energy differences between adjacent intermediates were computed using the Bennett acceptance ratio method (33); statistical uncertainties were estimated by dividing the data into 5 equal time intervals, and computing the standard deviation in the free energies between the intervals.

We also computed free energies for dihydroalprenolol bound to the β_2AR extracellular vestibule. Two different poses of dihydroalprenolol bound in the vestibule—pose 2 and pose 3 in Fig. 2—were selected from binding simulation 1 (Table S2); dihydroalprenolol had remained in each of these poses for over 100 ns during binding. The computed binding free energies were -7.1 ± 1.0 and -7.9 ± 1.2 kcal/mol for poses 2 and 3, respectively. These results indicate that the extracellular vestibule is a favorable ($K_D \approx 5$ μM) metastable binding site for the ligand on its path into the deeper orthosteric site.

1. Shaw DE, et al. (2009) Millisecond-scale molecular dynamics simulations on Anton. *Proceedings of the Conference on High Performance Computing, Networking, Storage and Analysis (SC09)* (ACM, New York).
2. Bowers KJ, et al. (2006) Scalable algorithms for molecular dynamics simulations on commodity clusters. *Proceedings of the ACM/IEEE Conference on Supercomputing (SC06)* (ACM, New York).
3. Dror RO, et al. (2009) Identification of two distinct inactive conformations of the β_2-adrenergic receptor reconciles structural and biochemical observations. *Proc Natl Acad Sci USA* 106:4689–4694.
4. Fahmy K, et al. (1993) Protonation states of membrane-embedded carboxylic acid groups in rhodopsin and metarhodopsin II: A Fourier-transform infrared spectroscopy study of site-directed mutants. *Proc Natl Acad Sci USA* 90:10206–10210.
5. Rosenbaum DM, et al. (2011) Structure and function of an irreversible agonist-β_2 adrenoceptor complex. *Nature* 469:236–240.
6. Darden T, York D, Pedersen L (1993) Particle mesh Ewald: An $N\log(N)$ method for Ewald sums in large systems. *J Chem Phys* 98:10089–10092.
7. Kräutler V, Van Gunsteren WF, Hünenberger PH (2001) A fast SHAKE algorithm to solve distance constraint equations for small molecules in molecular dynamics simulations. *J Comput Chem* 22:501–508.
8. Tuckerman M, Berne BJ, Martyna GJ (1992) Reversible multiple time scale molecular dynamics. *J Chem Phys* 97:1990–2001.
9. Shan Y, Klepeis JL, Eastwood MP, Dror RO, Shaw DE (2005) Gaussian split Ewald: A fast Ewald mesh method for molecular simulation. *J Chem Phys* 122:054101.
10. MacKerell AD Jr, et al. (1998) All-atom empirical potential for molecular modeling and dynamics studies of proteins. *J Phys Chem B* 102:3586–3616.
11. MacKerell AD Jr, Feig M, Brooks CL III (2004) Extending the treatment of backbone energetics in protein force fields: Limitations of gas-phase quantum mechanics in reproducing protein conformational distributions in molecular dynamics simulations. *J Comput Chem* 25:1400–1415.
12. Piana S, Lindorff-Larsen K, Shaw DE (2011) How robust are protein folding simulations with respect to force field parameterization? *Biophys J* 100:L47–L49.
13. Beglov D, Roux B (1994) Finite representation of an infinite bulk system: Solvent boundary potential for computer simulations. *J Chem Phys* 100:9050–9063.
14. Klauda JB, et al. (2010) Update of the CHARMM all-atom additive force field for lipids: Validation on six lipid types. *J Phys Chem B* 114:7830–7843.
15. Vanommeslaeghe K, et al. (2010) CHARMM General Force Field (CGenFF): A force field for drug-like molecules compatible with the CHARMM all-atom additive biological force fields. *J Comput Chem* 31:671–690.
16. Tu T, et al. (2008) A scalable parallel framework for analyzing terascale molecular dynamics simulation trajectories. *Proceedings of the ACM/IEEE Conference on Supercomputing (SC08)* (ACM, New York).
17. Humphrey W, Dalke A, Schulten K (1996) VMD—Visual Molecular Dynamics. *J Mol Graph Model* 14:33–38.
18. DeLano WL (2002) The PyMOL molecular graphics system (DeLano Scientific, San Carlos, CA). http://www.pymol.org.
19. Limbird LE, Lefkowitz RJ (1976) Negative cooperativity among β-adrenergic receptors. *J Biol Chem* 251:5007–5014.
20. Contreras ML, Wolfe BB, Molinoff PB (1986) Kinetic analysis of the interactions of agonists and antagonists with beta adrenergic receptors. *J Pharmacol Exp Ther* 239:136–43.
21. Czerlinski GH, Schreck G (1964) Fluorescence detection of the chemical relaxation of the reaction of lactate dehydrogenase with reduced nicotinamide adenine dinucleotide. *J Biol Chem* 239:913–921.
22. Nolte,H-J, Rosenberry TL, Neumann E (1980) Effective charge on acetylcholinesterase active sites determined from the ionic strength dependence of association rate constants with cationic ligands. *Biochemistry* 19:3705–3711.
23. Shenfeld DK, Xu H, Eastwood MP, Dror RO, Shaw DE (2009) Minimizing thermodynamic length to select intermediate states for free energy calculations and replica-exchange simulations. *Phys Rev E* 80:046705.
24. Severne Y, Kanarek L, Vauquelin G (1986) Agonist-mediated conformational changes of β-adrenoceptors could occur independent of functional coupling to Ns. *Naunyn Schmiedebergs Arch Pharmacol* 332:247–252.
25. Hoffmann C, Leitz MR, Oberdorf-Maass S, Lohse,MJ, Klotz K-N (2004) Comparative pharmacology of human beta-adrenergic receptor subtypes—Characterization of stably transfected receptors in CHO cells. *Naunyn Schmiedebergs Arch Pharmacol* 369:151–159.
26. Weiland GA, Minneman KP, Molinoff PB (1979) Fundamental difference between the molecular interactions of agonists and antagonists with the Beta-adrenergic receptor. *Nature* 281:114–117.
27. Wang JH (1951) Self-diffusion and structure of liquid water. II. Measurement of self-diffusion of liquid water with O^{18} as tracer. *J Am Chem Soc* 73:4181–4183.
28. Longsworth LG (1954) Temperature dependence of diffusion in aqueous solutions. *J Phys Chem* 58:770–773.
29. Caron MG, Lefkowitz RJ (1976) Solubilization and characterization of the β-adrenergic receptor binding sites of frog ethrocytes. *J Biol Chem* 251:2374–2384.
30. Boresch S, Tettinger F, Leitgeb M, Karplus M (2003) Absolute binding free energies: A quantitative approach for their calculation. *J Phys Chem B* 107:9535–9551.
31. Beutler TC, et al. (1994) Avoiding singularities and numerical instabilities in free-energy calculations based on molecular simulations. *Chem Phys Lett* 222:529–539.
32. Feller SE, Pastor RW (1999) Constant surface tension simulations of lipid bilayers: The sensitivity of surface areas and compressibilities. *J Chem Phys* 111:1281–1287.
33. Bennett CH (1976) Efficient estimation of free energy differences from Monte Carlo data. *J Comp Phys* 22:245–268.

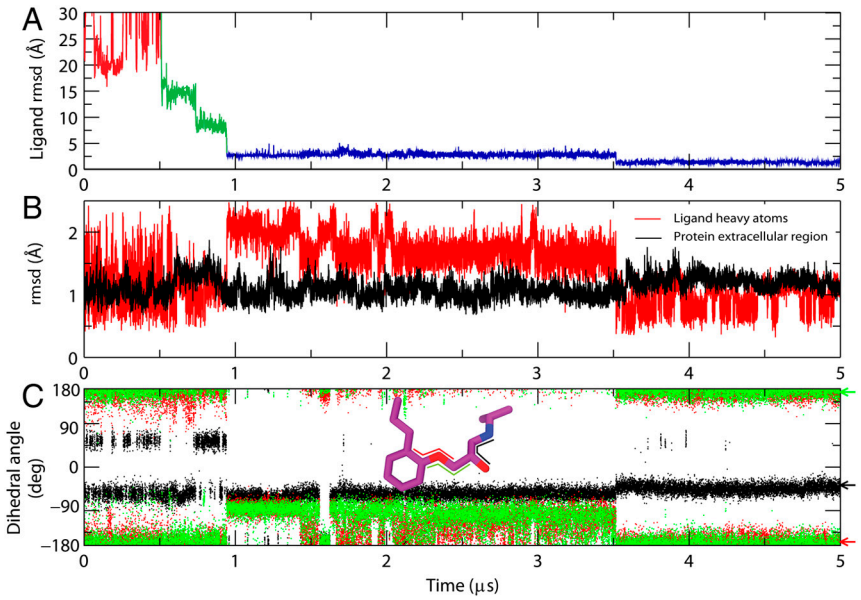

Fig. S1. The entry of alprenolol into the extracellular vestibule does not require any noteworthy structural change in the receptor or the ligand. (*A*) Rmsd of alprenolol in simulation from its position in the alprenolol–β_2AR crystal structure (PDB entry 3NYA), calculated after aligning on protein binding pocket C_α atoms (see *SI Text*). As in Fig. 2*B* of the main text, the colors indicate the location of the ligand relative to the protein: unbound (red), extracellular vestibule (green), and bound in the binding pocket (blue). (*B*) Rmsd of the protein extracellular region (black trace, backbone protein residues 82 to 118, 160 to 210, and 285 to 316) after aligning to the carazalol–β_2AR crystal structure (PDB entry 2RH1), and rmsd of alprenolol's non-hydrogen atoms (red trace) after aligning to corresponding atoms of the bound alprenolol in the 3NYA crystal structure. Incidentally, the reduced variance in ligand rmsd once bound to the protein appears to represent the constraining influence of the protein. The elevated ligand rmsd between approximately 1 and approximately 3.5 μs is due to the ligand being in the binding pocket but twisted near the beta-hydroxyl group (i.e., pose 4 of Fig. 2). (*C*) Three dihedral angles of alprenolol (trace colors correspond to the dihedrals indicated by the thick colored lines in the inset graphic). The data in these plots are from simulation 1 (Table S2).

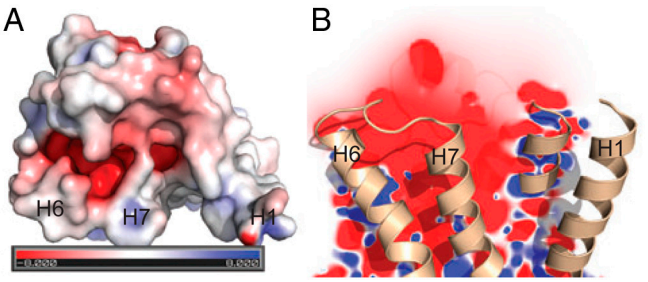

Fig. S2. Electrostatics do not present a barrier to ligand entry into the vestibule. The colors indicate the electrostatic potential (*A*) at the extracellular surface of the protein and (*B*) in a slice through the extracellular half of the receptor. The potential was determined by solving the linearized Poisson–Boltzmann equation at a salt concentration of 150 mM (1). Contours are in units of k_BT/e, where k_B is Boltzmann's constant, T is 310 K, and e is the charge of an electron. All simulated ligands carry a net +1 charge.

1 Baker NA, Sept D, Joseph S, Holst MJ, McCammon JA (2001) Electrostatics of nanosystems: Application to microtubules and the ribosome. *Proc Natl Acad Sci USA* 98:10037–10041.

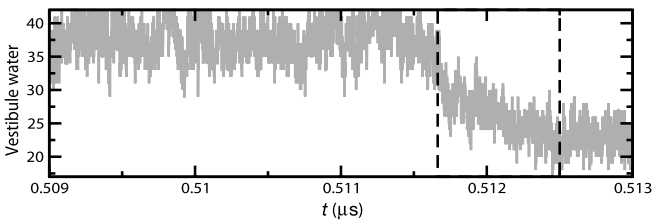

Fig. S3. Water molecules in the extracellular vestibule rapidly evacuate as alprenolol enters. The number of water molecules in the extracellular vestibule is plotted for simulation 1, "zoomed in" to the time when the ligand first enters and associates with this region. The time point when the ligand first enters the vestibule and the time point when it associates with the vestibule's surface are indicated by dashed vertical lines. During ligand entry, approximately 15 water molecules leave the vestibule in less than 1 nanosecond. Here, "vestibule water" (the vertical axis label) refers to the number of water oxygen atoms within an 8 Å radius of the point $(x,y,z) = (-28.7, -2.76, 12.3)$ after the C_α atoms of β_2AR residues 32–56, 70–94, 106–129, 150–170, 197–220, 275–295, and 307–325 were aligned to the crystal structure coordinates (PDB entry 2RH1).

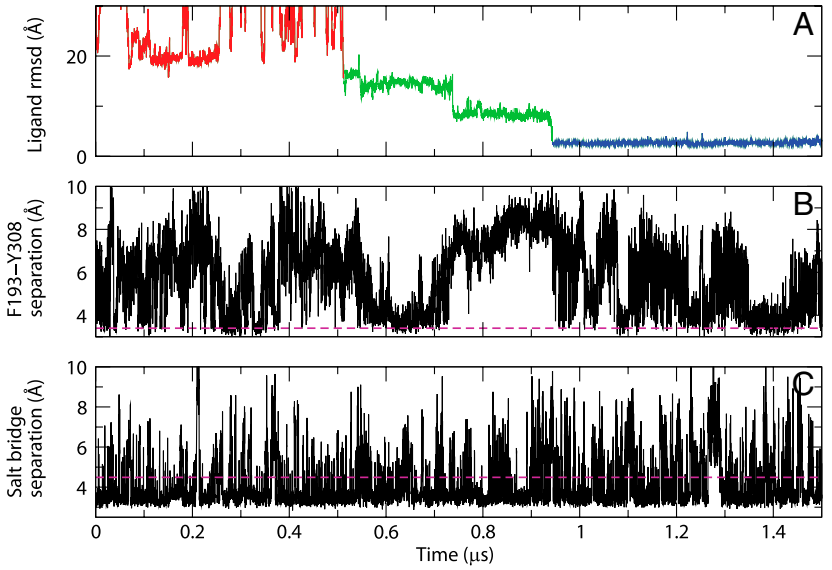

Fig. S4. Receptor conformational changes do not limit the rate of alprenolol movement from the vestibule into the binding pocket. Structural changes from the receptor's crystallographic conformation (in particular, separation of Phe193^{ECL2} from Tyr308$^{7.35}$, and breaking of the Asp192^{ECL2}–Lys305$^{7.32}$ salt bridge) occur before alprenolol moves from the vestibule into the binding pocket, but these changes do not appear to be rate-limiting. The ligand's rmsd from its final bound pose (*A*) is juxtaposed with (*B*) the minimum distance between the non-hydrogen atoms of the side chains of Phe193^{ECL2} and Tyr308$^{7.35}$ and (*C*) the distance between Asp192^{ECL2} C_γ and Lys305$^{7.32}$ N_ζ. While the ligand waits in the extracellular vestibule (approximately 0.52 to approximately 0.94 μs), the side chains of Phe193^{ECL2} and Tyr308$^{7.35}$ remain separated for approximately 200 ns (approximately 0.75–0.94 μs) and the salt bridge breaks and reforms over 200 times. The breaking and forming rates of he salt bridge are 10^8 and 10^9 s^{-1}, respectively (calculated with a salt bridge cutoff of 4.5 Å), while the rate of ligand entry into the binding pocket from the extracellular vestibule (estimated from residence times of ligands in the vestibule in multiple trajectories) is 10^6 s^{-1}. The dashed magenta lines in (*B*) and (*C*) indicate the values of these observables in the alprenolol–β_2AR complex crystal structure (PDB entry 3NYA). Data are from simulation 1.

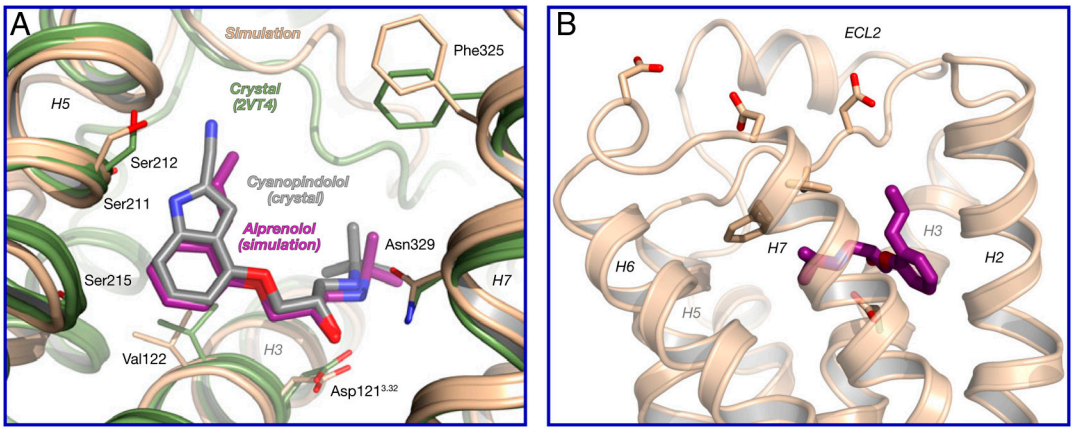

Fig. S5. Alprenolol binds spontaneously to β_1AR in unbiased molecular dynamics simulations, adopting the crystallographically observed pose in some simulations and an alternative pose in others. (*A*) Dihydroalprenolol-bound β_1AR pose from simulation 18 (tan) superimposed on the cyanopindolol-β_1AR complex crystal structure (PDB entry 2VT4; gray). (*B*) Dihydroalprenolol-bound β_1AR pose from simulation 21; this pose is similar to that of Fig. 2, pose 4′.

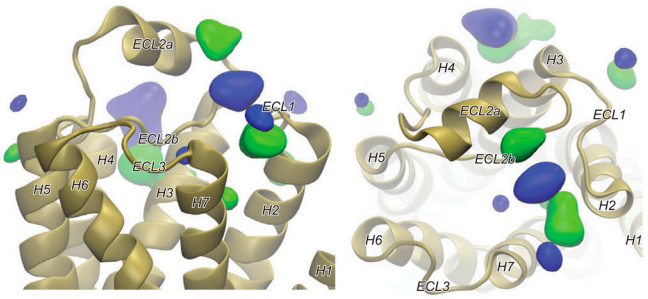

Fig. S6. Alprenolol aromatic ring and ammonium group occupancies in simulations without a binding event show other potential allosteric binding sites. Twenty percent isosurface of alprenolol ammonium group (blue) and ring center (green) over all simulations under conditions *A*–*C* (Table S1) in which an alprenolol molecule did not bind to the orthosteric site. Density maps were computed using the VolMap tool in VMD (17).

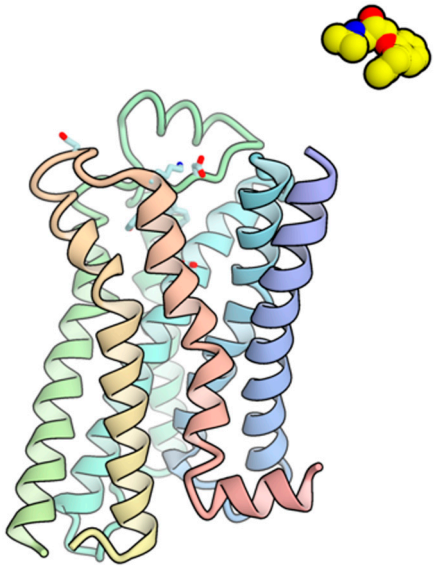

Movie S1 A movie of alprenolol binding to β_2AR, based on simulation 1. For clarity, the lipid bilayer, ions, and water molecules are not shown. The movie plays at 4.5 ns per frame until 0.98 μs, after which it plays at 22.5 ns per frame (i.e., five times faster). The Cartesian components of the protein C_α positions were smoothed using a Gaussian filter ($\sigma = 18$ ns). For the ligand, no smoothing was applied for the first 110 frames of the animation (time = 0.0–0.98 μs). For the remainder of the animation, both the Cartesian components of the ligand atom positions and the internal angles were smoothed using Gaussian filters, with σ values of 8.1 ns and 18 ns, respectively. The movie was created using OpenStructure (1).
Movie S1 (AVI)

1 Biasini M, et al. (2010) OpenStructure: A flexible software framework for computational structural biology. *Bioinformatics* 26:2626–2628.

Table S1. Simulation conditions and durations

Condition	Ligand	Na^+	Cl^-	Num.	Durations (μs)
β_2AR					
A	dihydroalprenolol	0	14	20	5.0, 10.9, 18.9, 1.0, 2.0, 1.0, 1.0, 1.0, 3.0, 3.0, 3.0, *1.0*, *1.0*, *1.0*, *1.0*, *1.0*, *5.0*, *9.0*, *1.0*, *1.5*
B	dihydroalprenolol	20	34	20	6.0, 3.0, 3.0, 1.0, 1.5, 1.0, 1.0, 1.0, 1.0, 2.0, 1.0, 1.0, 1.0, 1.0, 1.0, 5.0, 3.0, 5.0, 1.0, 1.0
C	alprenolol	0	14	10	1.0, 1.0, 1.0, 1.0, 1.0, 3.0, 1.0, 1.0, 1.0, 3.0
D	propranolol	0	14	21	1.0, 1.0, 1.0, 1.0, 1.0, 1.0, 5.0, 1.0, 1.0, 1.0, 1.0, 5.0, 1.0, 1.0, 1.0, 2.1, 1.0, 1.0, 2.6, 1.0, 5.0
E	isoproterenol	0	14	1	15.0
β_1AR					
F	dihydroalprenolol	1	19	10	10.7, 6.0, 6.0, 6.0, 1.0, 2.8, 6.0, 6.0, 1.0, 10.0

All simulations listed in this table were initiated with 10 ligands placed at arbitrary positions in the aqueous phase, each at least 30 Å away from the binding pocket. The third and fourth columns indicate the number of Na^+ and Cl^- ions in each simulation cell, whereas the fifth indicates the number of independent simulations performed under each condition. The durations shown in italics in condition A denote simulations in which weak (0.5 kcal mol^{-1} Å^{-2}) harmonic restraints were applied to the C_α atoms of residues 54–59, 68–73, 131–136, 148–153, 224–229, 267–272, and 323–328 to keep the protein centered and oriented in the simulation box; these restraints were imposed to facilitate certain analyses and did have any noticeable effect on the binding pathway. The single sodium ion in condition F is from the crystal structure of β_1AR.

Table S2. Simulations with binding events

Simulation	Ligand	Condition	Duration (μs)	Final pose	Other poses
β_2AR					
1	dihydroalprenolol	A	5.0	5	—
2	dihydroalprenolol	A	3.0	5	—
3	dihydroalprenolol	A	10.9	4′′	4′
4	dihydroalprenolol	A	4.0	5	—
5	dihydroalprenolol	A	10.0	4′	—
6	dihydroalprenolol	A	5.0	5	4′
7	dihydroalprenolol	A	9.0	4′	—
8	dihydroalprenolol	B	5.0	4′′	—
9	dihydroalprenolol	B	3.0	5	—
10	dihydroalprenolol	B	5.0	4′′	—
11	alprenolol	C	3.0	5	4′′
12	alprenolol	C	3.0	4′′	—
13	propranolol	D	5.0	4′′	—
14	propranolol	D	5.0	4′′	—
15	propranolol	D	5.0	5	4′, 4′′
16	isoproterenol	E	15.0	4	—
β_1AR					
17	dihydroalprenolol	F	10.7	4′	—
18	dihydroalprenolol	F	6.0	5	—
19	dihydroalprenolol	F	6.0	4′	—
20	dihydroalprenolol	F	6.0	4′	—
21	dihydroalprenolol	F	10.0	5	4′, 4′′

Letters in the "Condition" column refer to simulation conditions listed in Table S1. The "Final pose" column indicates the pose at the end of the simulation, whereas the "Other poses" column indicates other poses the ligand adopted while in the binding pocket. The symbols in these two columns refer to poses shown in Fig. 2.

Table S3. A majority of the solvent-accessible surface area lost by the protein and the ligand during the binding process is lost upon ligand entry into the extracellular vestibule.

	Average ligand SASA loss (Å^2)	Average protein SASA loss (Å^2)
Extracellular vestibule	338	165
Binding pocket	415	185

Entries in the table indicate the solvent-accessible surface area (SASA) loss relative to the state when all ligands are in bulk solvent. These SASA values (1) are computed from simulation 1 using the program AREAIMOL from the CCP4 program suite (2) and correspond to the hydrophobic surface area (i.e., carbon SASA) lost by the protein and the ligand.

1 Lee B, Richards FM (1971) The interpretation of protein structures: Estimation of static accessibility. *J Mol Biol* 55:379–400.
2 Collaborative Computational Project, Number 4 (1994) The CCP4 suite: Programs for protein crystallography. *Acta Cryst D Biol Crystallogr* 50:760–763.